Extreme Mechanics Letters 62 (2023) 102047

Contents lists available at ScienceDirect

Extreme Mechanics Letters

journal homepage: www.elsevier.com/locate/eml

Experimental and computational models for simulating the oral breakdown of food due to the interaction with molar teeth during the first bite

Georgios Samaras [a,*], Dimitrios Bikos [a], Christos Skamniotis [a], Philippa Cann [a], Marc Masen [a], Yannis Hardalupas [a], Josélio Vieira [b], Christoph Hartmann [c], Maria Charalambides [a]

[a] Department of Mechanical Engineering, Imperial College London, UK
[b] Nestlé Product Technology Centre, York, UK
[c] Nestlé Research, Lausanne, Switzerland

ARTICLE INFO

Article history:
Received 3 February 2023
Received in revised form 2 June 2023
Accepted 3 July 2023
Available online 7 July 2023

Keywords:
Gradient-enhanced damage model
Mesh dependency
First human oral bite modelling
Ductile damage

ABSTRACT

The first bite involves the structural breakdown of foods due to the interaction with teeth and is a crucial process in oral processing. Although *in vitro* experiments are useful in predicting the oral response of food, they do not facilitate a mechanistic understanding of the relationship between the intrinsic food mechanical properties and the food behaviour in the oral cavity. Computer simulations, on the other hand, allow for such links to be established, offering a promising design alternative that will reduce the need for time consuming and costly *in vivo* and *in vitro* trials. Developing virtual models of ductile fracture in soft materials, such as food, with random and non-predefined crack morphology imposes many challenges. One of the most important is to derive results that do not depend on numerical parameters, such as Finite Element (FE) mesh density, but only physical constants obtained through independent standard mechanical tests, such as fracture strain and/or critical energy release rate. We demonstrate here that this challenge can be overcome if a non-local damage approach is used within the FE framework. We develop a first bite FE modelling methodology that provides mesh independent results which are also in agreement with physical first bite experiments performed on chocolate. The model accounts for key features found in chocolate and a wide range of compliant media, such as rate dependent plasticity and pressure dependent fracture initiation strain. As a result, our computational methodology can prove valuable in studying food structure-function relationships that are essential in product development.

1. Introduction

First bite is the initial step of mastication and belongs in the general process of digestion. The first bite involves the structural breakdown of food due to the interaction with teeth and as a process is crucial since during breakdown, the newly exposed surface area that comes into contact with saliva increases, allowing for further chemical degradation by the saliva enzymes [1].

Several attempts have been made to physically replicate the chewing process in a laboratory environment, through apparatus that simulates the movement of the teeth and measures the reaction force using strain gauges [2,3]. Although the results obtained by such experimental set-ups are useful to characterise the food under investigation, it is difficult to derive physical insight that will allow an efficient food design [4]. For this reason, a design tool is needed which can perform virtual first bite simulations. A computational model allows for efficient product development and optimisation by providing a tool whose parameters can be easily changed and isolated such that new configurations can be quickly and efficiently tested [5].

The physiological conditions in the mouth during the first bite are important in creating a reliable FE model. Bite force is an important variable to investigate as it influences the fragmentation of the food. The most widely accepted recording device for measuring bite forces is the strain-gauge bite force transducer [6–8]. Biswas et al. [9] showed that the axial forces during biting can range between 77–2440 N and the lateral forces are less than 100 N. From measurements conducted in foods such as carrots and biscuits, forces were measured in the range 70–150 N [10]. The chewing speed is another parameter that plays an important role during the first bite [11,12]. Meullenet et al. [13] reported

* Corresponding author.
E-mail address: georgios.samaras17@imperial.ac.uk (G. Samaras).

https://doi.org/10.1016/j.eml.2023.102047

chewing speed ranging between 26–35.1 mm s^{-1}. Sánchez-Ayala et al. [14] used a cylindrical silicon test material similar to Buschang et al. [15] and the chewing speed measured was 26.2 mm s^{-1}. These values are somewhat higher than those reported by Yoshiba et al. [16] (19.4 mm s^{-1}), Gomes et al. [17] (16.8 mm s^{-1}) and Throckmorton et al. [18] (21.83 mm s^{-1}). The differences in these chewing rate values can be related to the type of food used, the shape of the specimens that the volunteers were asked to chew or the natural variations in humans [14]. The study of Bates et al. [19] gives a wider range between 19.3 mm s^{-1} and 40 mm s^{-1}. In the present study, the chewing speed used in the FE simulations is limited by the maximum speed (15 mm s^{-1}) that can be reached by a screw driven mechanical tester.

Several attempts have been made in the literature to simulate the initial stages of oral processing. Harrison et al. [20] used a coupled bio-mechanical-smoothed particle hydrodynamics (B-SPH) model that predicts the food breakdown due to the interaction of the food with saliva and anatomical structures of the mouth (tongue, teeth, cheeks). Although this study takes into account a more accurate scenario where the food interacts with more surfaces in the mouth, the constitutive model used was a simple elastic-perfectly plastic model coupled with a simple fracture criterion. Dejak et al. [21] presented a FE model to analyse the stresses induced by the molar teeth during chewing of morsels using various elastic moduli. Skamniotis et al. [5] demonstrated a FE model in a dynamic Explicit FE analysis solver that simulates the first bite of pet food. In this latter model a pressure dependent viscoplastic material model was used coupled with an isotropic ductile damage evolution law that is driven by the critical energy release rate of the food. The results were promising, although a local damage model was used, making the simulation results mesh dependent.

An important aspect of simulating the food fragmentation during the first bite is the selection of an appropriate damage framework. In the local Continuum Damage Mechanics (CDM) model (e.g. ductile damage model in the commercially available FE software ABAQUS [22]) the damage parameter depends only on the strain state at each material point. This causes the numerical simulations to exhibit a pathological mesh dependence and the damage parameter tends to increase as the mesh is refined leading to unreliable results [23]. The limitation is derived from the fact that when investigating the shear band formation using CDM, the numerical solutions suffer from ill-posed mathematics and the governing partial differential equations (PDEs) lose ellipticity (from elliptic to hyperbolic) [24]. The absence of an internal material length in the classical continuum theory, causes the characteristic element length to become the material length.

The FE calculation using local CDM has no physical meaning as the predictions of the crack propagation depends on the element size which is not a material property, such as an internal length scale. A technique to resolve the mesh dependency problem is by extending the classic CDM theory to include a characteristic length of the material, that is related to inter-void distance or the grain size of the material's microstructure [24]. Such extension is performed through strain gradient or non-local models [25]. In non-local models, the microstructure interaction around a material point is introduced, where the stress response of a material point is assumed to depend on the state of its neighbourhood. A non-local variable is defined as a weighted average at a point and the size of the neighbourhood that is assumed to influence the state of the material point is defined through the internal material length. Kröner [26] and Eringen and Edelen [27] applied the non-local theory for an elastic material. This theory was further developed and applied into continuum damage mechanics by the work of Pijauder-Cabot and co-workers [28]. The direct averaging procedure of the non-local models requires significant computational effort making these models inefficient to use. For this reason, strain gradient theories are used as an approximation to the non-local models. The strain gradient theory approximates the non-local models by Taylor expanding the integral form that averages the strain field over the surrounding volume of a material point [29].

The current study presents an FE model of the first bite on chocolate, developed based on the explicit Johnson Cook constitutive law coupled with a non-local damage model. The numerical results are compared and validated against experimental data obtained from a physical replicate of the mastication model, while the constitutive model is calibrated against uniaxial monotonic mechanical tests under different modes of deformation (compression and tension [30]). The purpose of the FE model is twofold; initially, it can be used as a reliable tool to study the fragmentation paths for the chocolate, and it can also be used to understand how changes in the mechanical properties through changes in the microstructure (e.g. micro-aeration in chocolate [30]) influence the mechanical breakdown during the first bite. It is for the first time that a strain-gradient enhanced damage model is applied to study food fragmentation, whereas previous studies used simpler mesh-dependent damage laws. Our study aims to fill this gap in the literature and provide a computational tool that can be used to examine reliably the fragmentation of food without the results being influenced by the mesh density. Moreover, the parameters used in the *in silico* model have been calculated through independent mechanical test, which allows the model to be applied to other types of foods.

2. Materials and methods

2.1. Materials and mechanical characterisation

The chocolate used in the study of Bikos et al. [31] was also used here, as the material to be subjected to the first bite. The chocolate had a typical composition of 44 wt% sugar particles, 27 wt% cocoa fat, 10 wt% whole milk powder, 6 wt% non-fat cocoa solids, and 0.3% sunflower lecithin, and was provided by the Nestlé-Product Technology Centre (NPTC) in York, UK.

The mechanical properties of the chocolate were measured by Bikos et al. [30,32] and will be used in the current study to calibrate the constitutive model. The tensile and compressive experimental data are presented in Fig. 1 in the form of true stress versus true strain as a function of true strain rate. Results from replicate tests showed only small variations so the error bars were very small (not shown in Fig. 1 [30]).

2.2. Experimental rig model for the first bite

An experimental rig was used to provide *in vitro* data for the *in silico* model validation. A digitised adult male 3D skull, generated using X-ray computed tomography, was used to extract the geometry of a pair of the two last molar teeth (Fig. 2(a)). The data were provided by Nestlé as an STL format, which was processed in SOLIDWORKS. In order to aid the experimental procedure and simplify the model, the last two sets of molar teeth as shown in Fig. 2(a) were extracted from the full jaw geometry and were tilted in order to become normal to the laboratory surface. To isolate the pair of the two molar teeth, the upper (maxilla) and lower (mandible) jaws were cropped and the free edges were covered to create a closed surface that allowed the created volumes to be 3D printed.

In order to attach the pair of molar teeth extracted from the full jaw model onto a 5584 universal Instron universal testing machine, adaptors were designed in order to provide the proper alignment with the 2 kN load cell axis to eliminate any moments.

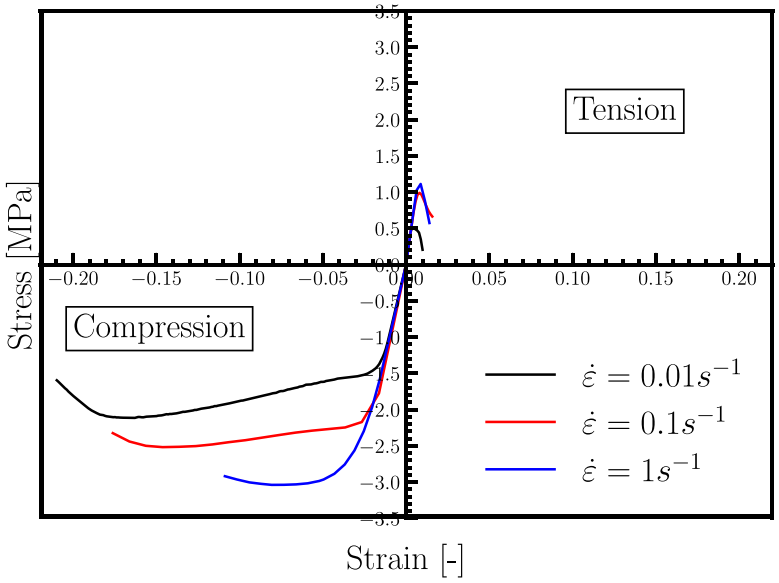

Fig. 1. Comparison between compression and tension experimental true stress versus true strain data. Data adopted from the study of Bikos et al. [30,32]. The experimental data correspond to three different true strain rates $\dot{\varepsilon} = 0.01, 0.1$ and $1\,s^{-1}$.

The adaptors were 3D printed together with the molar teeth as one continuous part using a Stratasys Dimension 1200es machine and were made of Acrylonitrile Butadiene Styrene (ABS).

In the present study, the assumption that the trajectory of the mandible remains linear during the duration of the first bite was adopted, similar to the study of Skamniotis et al. [5] and Evans and Fortelius [33]. This approximation is adopted in order to simplify the model, since there are already many parameters that are taken into account such as the non-local damage model and the strain rate dependent behaviour of the material. Some studies in the literature take into consideration more physical parameters that might influence the structural breakdown of food, but more simplified material and damage models were used [1,20,21]. Also this simplification allows the comparison of the FE model, described in Section 3.4, with an experimental set-up developed in a conventional uniaxial testing machine, without the need of a more sophisticated multiaxial testing machine.

The experimental set-up is shown in Fig. 2(b). The set-up consists of the mandible placed on the top moving part of the Instron and the maxilla placed on the bottom fixed head. This configuration better mimics the physiological condition where the mandible moves and the maxilla is fixed. An optical camera was used to capture the fragmentation. The chocolate specimens were cut using a razor blade in lengths of 10 mm. The width of 14 mm and height of 8 mm were fixed from the manufacturing process of the specimens and overall the cross sectional area was 140 mm^2. These dimensions correspond to a mass of 1.5 g, which is consistent with the study of Lucas and Luke [34] and in the range of the mouthful size [35–37]. The specimens were positioned as shown in Fig. 2(b), having contact with both the two last molar teeth of the upper and lower jaw.

Three speeds of, $\dot{\delta} = 8, 10, 15\,mm\,s^{-1}$, were tested to examine the effect of rate dependency on the chocolate specimens. Although the mastication speed, recorded in the literature, is closer to the latter (higher) test speed, additional speeds were examined to test the repeatability of the results and verify the rate dependent behaviour of the material. The opening between the upper and lower teeth was specified by the height of the specimen (∼8 mm) and the initial position was adjusted before each test due to a slight variation in the height of the samples due to the manufacturing process. The displacement, δ, was allowed to increase until $\delta = 7$ mm allowing the test to terminate 1 mm before the upper and lower teeth came into contact to avoid damage to the load cell. Each test was repeated five times for each speed.

3. Material modelling

3.1. Modified Johnson–Cook constitutive model

We use an isotropic hardening and rate dependent plasticity law with a Von Mises yield surface defined by the following Johnson–Cook expression:

$$\sigma_y = \left[A + B\left(\varepsilon^p_{eq}\right)^n\right]\left[1 + C\ln\left(\frac{\dot{\varepsilon}^p_{eq}}{\dot{\varepsilon}_0}\right)\right] \tag{1}$$

The terms A, B and n control the hardening behaviour and the terms C and $\dot{\varepsilon}_0$ the rate-dependent behaviour, whereas ε^p_{eq} is the equivalent plastic strain.

The Johnson–Cook model was calibrated using the compression data in Fig. 1, as this allowed calibration to higher strains. The tensile experimental data were however employed for the definition of the plastic strain at fracture as a function of the triaxiality factor (see Section 3.2). During the first bite process, the teeth apply compressive loads hence the compression data are important. However, it is argued that fracture occurs due to the lateral tensile deformation, hence the fracture data in tension are also needed.

The modified Johnson–Cook constitutive model was implemented in ABAQUS/Explicit through a VUMAT subroutine [30]. The part until the maximum stress point of the compression experimental data at each strain rate in Fig. 1 was initially considered, excluding the softening part. The softening part of the stress–strain curves will be considered for the calibration of the parameters that are involved in the damage evolution law (see Section 3.2).

The Young's modulus, E, was calculated from the gradient of the elastic region of the compression experimental data of Fig. 1 and the Poisson's ratio, ν, was taken from the study of Bikos et al. [30]. All the calibrated parameters are given in Table 1. Fig. 3 depicts a comparison of the stress–strain data obtained from compression experiments and the output from the FE analysis of a single element subjected to uniaxial loading. The Johnson–Cook model calibrated according to Table 1 lies in good agreement with the experimental data.

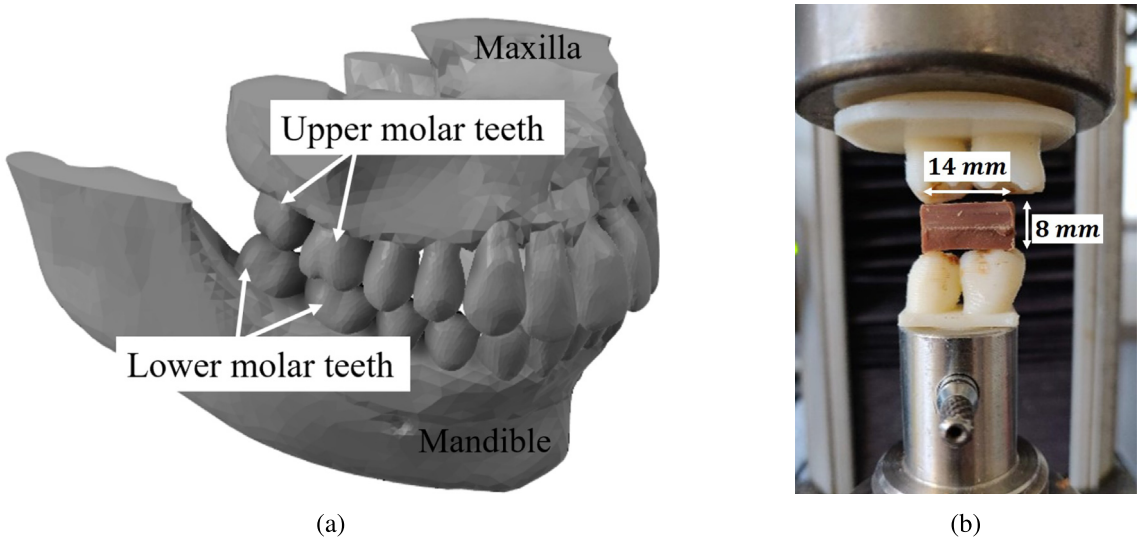

Fig. 2. (a) Upper and lower molar teeth used in the FE simulation after segmentation from the full jaw geometry. (b) Experimental set-up consisting of the 3D printed upper and lower molar teeth with their adaptors, the Instron universal machine and the chocolate specimen placed between the teeth. The specimen dimensions are also shown. The horizontal line that is visible in the chocolate frames is due to the razor used to cut the specimens to the desired geometries.

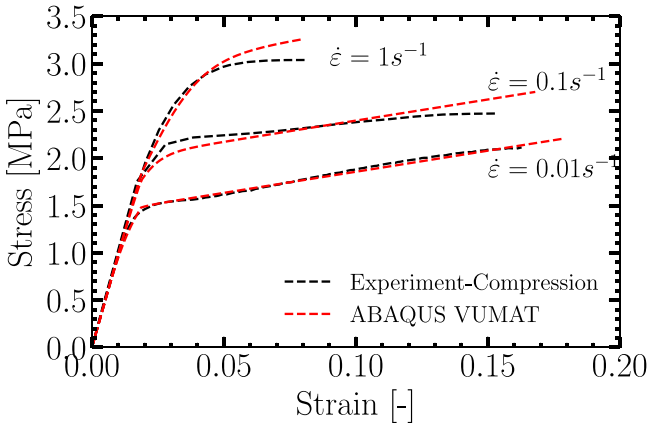

Fig. 3. Comparison between the Johnson–Cook model implemented in VUMAT and the experimental data in compression [30].

3.2. Damage model

Although several damage models exist in the literature [38], a version of the modified damage model of Bai and Wierzbicki [39] is adopted in the current study. This selection allows a direct comparison with the built-in ductile damage model of ABAQUS. The linear dissipation-energy-based damage evolution law is given by [22]:

$$\dot{d} = \frac{\sigma_{y,i} l}{2G_f} \dot{\varepsilon}^p_{eq} \tag{2}$$

where $\sigma_{y,i}$ is the yield stress at the damage onset, l is an internal length and G_f is the critical energy release rate with dimensions of energy per unit surface area [J/m^2]. Overall the damage evolution law is controlled by a damage initiation equivalent plastic strain, $\varepsilon^p_{eq,i}$, and an energy based evolution law, based on G_f; including the triaxiality parameter, η, it is written as:

$$d = \begin{cases} 0; & \varepsilon^p_{eq} \le \varepsilon^p_{eq,i} \\ \int_{\varepsilon^p_{eq,i}}^{\varepsilon^p_{eq,f}} \frac{\sigma_{y,i} l}{2G_f} \, \mathrm{d}\varepsilon^p_{eq}; & \varepsilon^p_{eq,i} < \varepsilon^p_{eq} < \varepsilon^p_{eq,f} \\ d_{cr} & \varepsilon^p_{eq} = \varepsilon^p_{eq,f} \end{cases} \tag{3}$$

Table 1
Material properties for the FE simulations.

Parameter	Value
Density, ρ [kg m^{-3}] [30]	1300
Elastic modulus, E [MPa]	100
Poisson's ratio, ν [–]	0.49
A [MPa]	1.35
B [MPa]	3.5
C [–]	0.05
n [–]	0.8
$\dot{\varepsilon}_0$ [s^{-1}]	0.01
Internal length, l [mm]	0.08
d_{cr}	0.1

where $\varepsilon^p_{eq,f}$ is the equivalent plastic strain at failure and complete damage is achieved when the damage parameter d reaches a critical value d_{cr}. The strain at the initiation of bulk fracture, $\varepsilon^p_{eq,i}$, corresponds to the point of maximum stress, $\sigma_{eq,i}$, in the stress–strain curves, before softening is observed. The equivalent plastic strain is needed in the damage evolution law and is calculated as:

$$\varepsilon^p_{eq,i} = \varepsilon_{eq,i} - \frac{\sigma_{eq,i}}{E} \tag{4}$$

with the index i indicating the damage initiation, E is the Young's modulus corresponding to the gradient of the elastic part, and the value of $\varepsilon_{eq,i}$ corresponds to the strain where the maximum stress, $\sigma_{eq,i}$, is observed in the stress–strain data of Fig. 1. The equivalent plastic strain at the end of failure, $\varepsilon^p_{eq,f}$, is calculated through the damage evolution law that is controlled by the critical energy release rate, G_f, measured experimentally by Bikos et al. [30].

The influence of triaxiality on the damage evolution should be considered as well, since during chewing there are multiple stress states [40]. The Young's modulus, E, in Eq. (4), was estimated from the compressive experimental data of Fig. 1 and was considered the same for tension as well. For uniaxial compression, $\eta = -1/3$, the value of $\varepsilon^p_{eq,i}$ was found from using Eq. (4) and the maximum points in the compressive part of the stress–strain data in Fig. 1. For tension, $\eta = 1/3$, Eq. (4) was used this time with the maximum points in the tensile stress–strain data. In both cases, the value of $\varepsilon^p_{eq,i}$ was given as a function of applied true strain rate. Although data for shear failure strain was not available, the damage criterion was extended to include the equivalent

Table 2
Equivalent plastic strain at damage onset for different stress states and strain rates.

$\varepsilon^p_{eq,i}$	η	$\dot{\varepsilon}$ (s^{-1})
0.16	−1/3	0.01
0.0058	0	0.01
0.006	1/3	0.01
0.154	−1/3	0.1
0.0069	0	0.1
0.008	1/3	0.1
0.08	−1/3	1
0.0078	0	1
0.009	1/3	1

plastic strain in shear, $\varepsilon^{p,s}_{eq,i}$, for each strain rate $\dot{\varepsilon}$. The equivalent plastic strain in shear ($\eta = 0$) is approximated using Eq. (5), and substituting $\varepsilon^p_2 = 0$ and $\varepsilon^p_1 = -\varepsilon^p_3 = \varepsilon^{p,t}_{eq,i}$, with $\varepsilon^{p,t}_{eq,i}$ representing the equivalent plastic strain at the damage onset in tension.

$$\varepsilon^p_{eq} = \frac{\sqrt{2}}{3}\left[\sqrt{\left(\varepsilon^p_1 - \varepsilon^p_2\right)^2 + \left(\varepsilon^p_2 - \varepsilon^p_3\right)^2 + \left(\varepsilon^p_3 - \varepsilon^p_1\right)^2}\right] \tag{5}$$

The correlation between the equivalent plastic strain in shear at the damage onset $\varepsilon^{p,s}_{eq,i}$, and the equivalent plastic strain in tension at the damage onset is then calculated as $\varepsilon^{p,s}_{eq,i} = \frac{\sqrt{3}}{2}\varepsilon^{p,t}_{eq,i}$, similar to Skamniotis et al. [41]. The equivalent plastic strains at the damage onset for different strain rates and stress triaxiality values are shown in Table 2.

The critical value of the damage parameter d_{cr} needs to be calibrated against the experimental data. The calibration methodology used by Lian et al. [42] is also applied in the present study. The critical energy release rate, G_f, was taken from single edge notched bending (SENB) tests and a detailed description is given by Bikos et al. [30]. The G_f value of the chocolate was reported to be in the range 8–12 J/m^2 for the different speeds and an average value of $10\,J/m^2$ is adopted for the damage evolution law of Eq. (3). The latter together with the equivalent plastic strain at the onset of damage, $\varepsilon^p_{eq,i}$, provide a direct connection to material properties that are independently measured and used to define damage evolution. It is worth noting that in the present study, the critical energy release rate has a physical meaning and is not used as a calibration parameter.

The damage law of Eq. (3) needs to be calibrated against the parameters d_{cr} and l, following the methodology of Lian et al. [42]. These two parameters are related to the damage propagation and can be calibrated by fitting the stress–strain curves from simulations to the experimental data. A single 3D element was subjected to compression and is used for the calibration of the d_{cr} and l. The experimental and numerical stress–strain curves are compared in Figs. 4(a) and 4(b). The numerical stress–strain curves at $\dot{\varepsilon} = 0.01, 0.1$ and $1\,s^{-1}$ for different l values and $d_{cr} = 1$ are shown in Fig. 4(a) and a value of $l = 0.08$ mm predicts well the onset of the softening branch of the curve. Afterwards, the same simulations were repeated keeping constant the already calibrated value of l and changing the value of the d_{cr} (Fig. 4(b)), which controls the equivalent plastic strain at failure (element deletion). A value of $d_{cr} = 0.1$ is considered sufficient for the proper calibration. Both values are calibrated for the highest strain rate, $\dot{\varepsilon} = 1\,s^{-1}$, that was experimentally tested, since the chewing rates existing in the mouth during the first bite are even higher than the available experimental data. Although l and d_{cr} were calibrated for $\dot{\varepsilon} = 1\,s^{-1}$, the calibrated values provided the lowest mean squared error for $\dot{\varepsilon} = 0.01\,s^{-1}$ and $\dot{\varepsilon} = 0.1\,s^{-1}$. All the parameters are summarised in Table 1.

3.3. Extension to non-local damage model

To overcome the mesh dependent problem of the continuum damage models, we introduce a gradient-enhanced damage model [43]. Peerlings et al. [44] derived an implicit equation according to which the non-local equivalent plastic strain, e^p_{eq}, is calculated as:

$$e^p_{eq} - l_{ch}\nabla^{(2)}e^p_{eq} = \varepsilon^p_{eq} \quad \text{in} \quad \Omega \tag{6}$$

where ε^p_{eq} is the local equivalent plastic strain, l_{ch} is the internal characteristic length with dimensions of length and Ω is the occupied domain. Eq. (6) is a Helmholtz type equation and a boundary condition must be provided in order to fix the solution. As proposed by Peerlings et al. [44], the following natural boundary condition is introduced and solved together with Eq. (6).

$$\frac{\partial e^p_{eq}}{\partial n} \equiv \mathbf{n}\cdot\nabla e^p_{eq} = 0 \quad \text{on} \quad \partial\Omega \tag{7}$$

where $\mathbf{n}$ is the unit outward normal vector to the surface $\partial\Omega$. Eq. (6) defines the non-local equivalent plastic strain implicitly in terms of the local plastic strain and together with the boundary condition of Eq. (7) they formulate the boundary value problem that needs to be solved.

We implement the methodology presented in detail in the study of Papadioti et al. [45] to calculate the non-local equivalent plastic strain. This methodology is based on the study of Seupel et al. [46] who coupled the user subroutines UMAT and HETVAL in the ABAQUS/Standard solver in order to calculate the non-local equivalent plastic strain. In our application, we take advantage of the similarities between Eq. (6) and the transient heat transfer equation, given by:

$$k\nabla^{(2)}T + r = \rho c\dot{T} \tag{8}$$

where c is the specific heat, T is the temperature, k is the thermal conductivity, r is the heat supply per unit volume and ρ is the density [22]. Comparing Eqs. (6) and (8) there is a direct correlation between the non-local equivalent plastic strain, e^p_{eq}, and the temperature, T. It is, then, possible to use the VDFLUX subroutine, to solve the non-local problem, by adjusting the following parameters:

$$T \leftrightarrow e^p_{eq}, \quad k \leftrightarrow l_{ch}, \quad r \leftrightarrow \varepsilon^p_{eq} - e^p_{eq} \tag{9}$$

The transient heat transfer equation (8) is already implemented in the VDFLUX subroutine which can be coupled with the constitutive equations in the VUMAT. The reader is referred to the study of Papadioti et al. [45] for a detailed discussion regarding the computational aspects that should be taken into account when using the transient heat transfer equation to solve Eq. (6).

It is worth noting that, special care should be taken regarding the time increment of the explicit analysis. The time increment in the coupled temperature–displacement analysis is computed according to Eq. (10) and depends on the density, ρ, the element size, $\Delta\ell_{el}$, the thermal conductivity, k, and the specific heat, c.

$$\Delta t > \frac{\rho c}{6k}\Delta\ell^2_{el} \tag{10}$$

From those parameters, only the specific heat does not have a physical meaning in our application and is chosen according to Eq. (11) in order allow the model to converge in a reasonable computational time.

$$\rho c\dot{e}^p_{eq} < \text{TOL} \tag{11}$$

where $\text{TOL} < 10^{-4}$ is a reasonable value for simulations where the elastic strain rates are small [45]. Therefore, it should be clarified here that the specific heat does not have any physical meaning, but it is selected in order to satisfy Eq. (11), taking

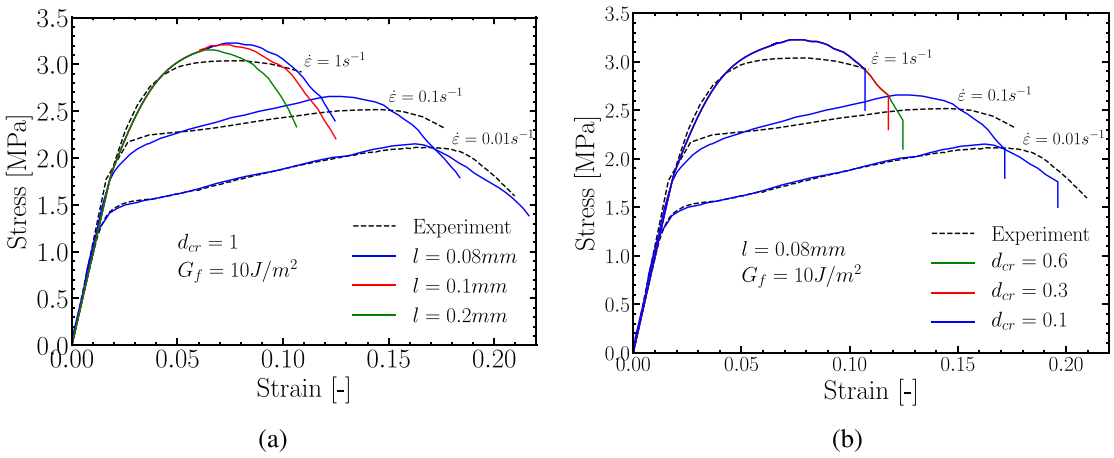

Fig. 4. Comparison between experimental [30] data and FE stress–strain results. For the numerical results, the VUMAT has been coupled with the local damage model for a single element in tension at three strain rates, for (a) the calibration of parameter l (b) the calibration of parameter d_{cr}.

into account the material density, ρ, and the applied strain rate, $\dot{e}^p_{eq}$. For the simulation of the first bite the specific heat was selected as 10^{-4} s/(kg/m^3). The internal characteristic length, l_{ch}, which is a calibration parameter that depends on the size of the food specimen was chosen as $l_{ch} = 0.1$ mm following the study of Papadioti et al. [45] who suggested that the l_{ch} is 1% of the specimen's length scale (here $\simeq$10 mm). The user material subroutine VUMAT in ABAQUS/Explicit together with a dynamic temperature displacement analysis is employed with a maximum time step $\Delta t = 10^{-5}$ s.

3.4. FE simulation model

The 3D geometry of the pair of molar teeth, used in the experimental Section 2.2, was imported in ABAQUS via using discrete rigid surfaces for the teeth and a deformable part for the food specimen, according to the dimensions used in the experimental study (see Fig. 5(a)). At this point, it is worth noting that the 3D printed teeth are considered as rigid, since the ABS is significantly stiffer than the chocolate ($E_{ABS} \approx 1.9-2$ GPa $> E_{ch} \approx 0.1$ GPa [47]). In addition to that, a compliance test was employed to correct for the machine's compliance and to eliminate any effects that a possible deformation of the ABS has due to interaction with the chocolate. The maxilla and the mandible were attached on the Instron machine and the test was conducted without the presence of a chocolate sample. The measured compliance is not related to the chocolate sample's deformation and it was therefore deducted from the force–displacement data when the chocolate was tested, providing the results shown in 6.

The upper and lower jaws were meshed with 23 742 four-node 3D bilinear rigid quadrilateral elements (R3D4), whereas the food specimen was meshed with 140 000 eight node thermally coupled bricks, trilinear displacement and temperature elements (C3D8T) [22]. A detailed discussion regarding the mesh sensitivity of the model will be provided in Section 4.2. A fully coupled thermal-stress analysis in ABAQUS/Explicit is chosen for the implementation of the non-local damage model, although there is no consideration of temperature in the model. As already mentioned, the heat transfer equations are integrated for the calculation of the temperature that plays the role of the non-local equivalent plastic strain.

Another important parameter in the FE simulation of the first bite is the definition of contact between the teeth and the specimen. The general contact option of ABAQUS/Explicit was used, which identifies surfaces in the 3D model assembly and generates contact forces to resist unreasonable penetrations. In the FE model, all the exterior and interior elements of the chocolate sample were assigned an element-based surface which was included in the contact domain. Thus, all the elements that consist the sample volume are allowed to be in contact between themselves (self-contact) as well as in contact with the teeth surface. The self contact parameter was necessary in this study since the final fragmentation of the specimen, driven by the element deletion, could cause some elements of the food specimen to come to contact with each other.

We selected the Coulomb friction model with a single parameter (coefficient of friction) to keep our models as simple as possible. The friction coefficient between the teeth and the food specimen plays an important role and influences significantly the results of the first bite simulation. The tangential interaction behaviour available in ABAQUS [22] was applied through the penalty contact option. Due to the lack of information regarding the coefficient of friction between the 3D-printed teeth and the solid chocolate (at 23 °C), tribology experiments on the same chocolate, presented in a previous study [48] were used as a guide in order to get a preliminary indication of the coefficient of friction. According to that study, the coefficient of friction between the molten chocolate (at 37 °C) and the polydimethylsiloxane (PDMS) (tongue substrate) was measured as $\mu = 0.42$ in dry conditions (no artificial saliva present). The ABS 3D printed surface was noticeably rougher than the PDMS so the coefficient of friction implemented in the FE models was assumed to be higher than $\mu = 0.42$ and taking into account a similar model developed by Skamniotis et al. [5] in the mastication of pet food, a parametric analysis for μ in the range 0.5-0.8 was conducted. It is worth noting that the measurement of the coefficient of friction between 3D-printed molar teeth and chocolate was not possible due to the complex geometry and topography of the teeth. This does not allow the use of the 3D-printed teeth in standard tribometers.

Regarding the boundary conditions of the chewing model, the maxilla was constrained in all translations and rotations, whereas the mandible was fixed in all translations, besides the z-axis (see Fig. 5(a)), and all rotations. It is worth noting that in Fig. 5(a) the maxilla appears on the bottom and the mandible at the top of the assembly. This was in order to have a direct comparison with the experimental set-up, where the mandible was attached on the top moving head of the Instron whereas the maxilla was placed at the bottom fixed head. This is the reason why the model appears rotated by 180°.

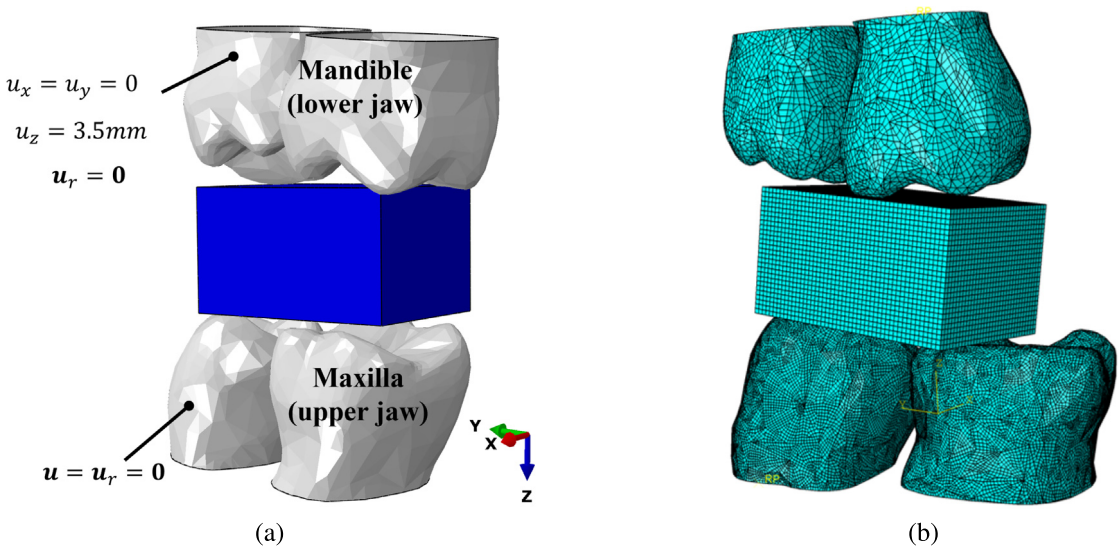

Fig. 5. (a) FE model assembly with the exact position of mandible, maxilla and food. The model appears rotated by 180° to be consistent with the experimental set-up. (b) FE model assembly with mesh discretisation. A denser mesh was applied to the maxilla due to the more uneven surface of the 3D-scanned geometry.

4. Results

4.1. First bite experimental results

Fig. 6 depicts the force–displacement data obtained for the three different speeds from the tests shown in Fig. 2(b). The error bars correspond to the maximum and minimum values across the five repeats of each test. There was a very good repeatability in all tests as shown in Fig. 6. Points A, B, C correspond to video frames from the experiment as shown in Fig. 10. For all speeds, there is an initial non-linear increase in force, followed by a sudden drop. The maximum force value corresponds to the fracture of the specimen due to the contact with the teeth. This force decrease is followed by another increase, which is a result of the compression of the already broken pieces in between the teeth. It is worth noting that the main interest of the current study is to capture the fragmentation of the specimen and for this reason the FE model will investigate the force–displacement response only until the specimen is considered as fully fractured, so until the sudden drop of the forces, corresponding to point *C* in Fig. 6. It is evident that increasing speed results in higher forces required for food breakdown, attributed to the rate dependent nature of the chocolate. For the highest speed of, $\dot{\delta} = 15\,\mathrm{mm\,s^{-1}}$, which is as already stated the most relevant to the human oral process, the maximum force drops from 59.8 N to 22.3 N after point *C*.

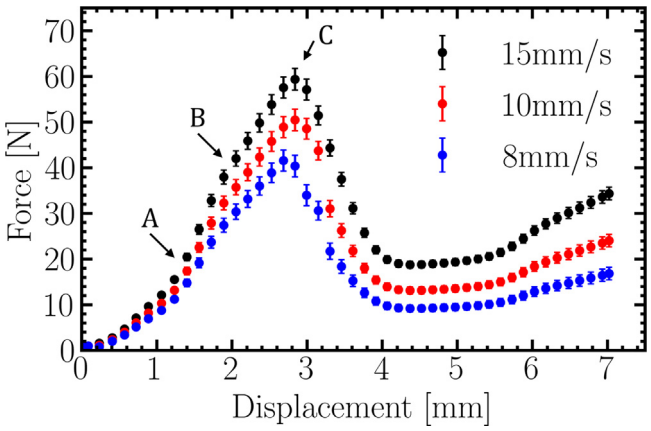

Fig. 6. Force–displacement data obtained from the experimental set-up. The results from three different chewing speeds are presented. Points A, B, C correspond to video frames from the experiment as shown in Fig. 10.

4.2. FE simulation results

In this section the force–displacement data computed from the simulations will be compared with the experimental results. Different coefficient of friction values will be examined and the FE model output will be compared with video frames of the experiment capturing the fracture of the specimen due to the interaction with the molar teeth. In addition, the efficiency of the non-local damage model will be investigated, through a comparison between the local and the non-local damage models.

Different coefficient of friction values ranging between $\mu = 0.5$-0.9, were tested and the force–displacement results at $\dot{\delta} = 15\,\mathrm{mm\,s^{-1}}$ are shown in Fig. 7. Increasing the coefficient of friction value resulted in higher forces for food fracture, as expected. In these simulations, the non-local damage model was applied and the coefficient of friction $\mu = 0.8$ was found to agree with the experimental observations, whereas a further increase of the coefficient of friction, $\mu = 0.9$, leads to a more brittle breakdown response (sudden drop in force). Therefore, the value of $\mu = 0.8$ was kept constant for the rest of the simulations of the chocolate samples.

Damage laws based on the continuum damage mechanics theory suffer from mesh dependency. This is evident in Fig. 8 where a coarse (100 000 elements) and a dense (140 000 elements) mesh discretisation of the food specimen are compared. The force–displacement data obtained from the local damage model depend on mesh density; as the mesh becomes more dense, higher forces are obtained. This behaviour results in different fragmentation paths implying that the FE model with the local damage law is unreliable for predicting the fracture. The mesh dependency is overcome by the implementation of the non-local damage law driven by the non-local equivalent plastic strain through the VDFLUX subroutine. The blue and the red continuous scatter lines correspond to the same mesh densities as the ones used with the local damage model depicted with red and blue dashed scatter lines, and a similar force–displacement trend is obtained, implying the mesh objectivity of the results. It is worth noting that, benchmark tests on induced shear band specimens, similar

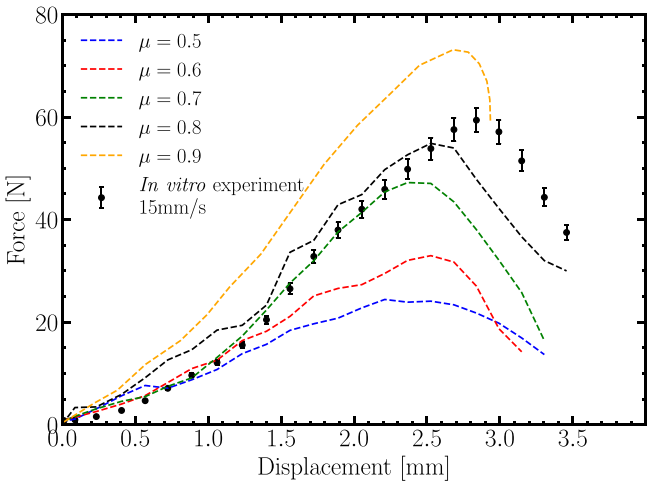

Fig. 7. Comparison of the experimental and FE force–displacement data for different values of friction coefficient for the non-aerated chocolate. The non-local damage model and a mesh with 140 000 elements were used for these simulations.

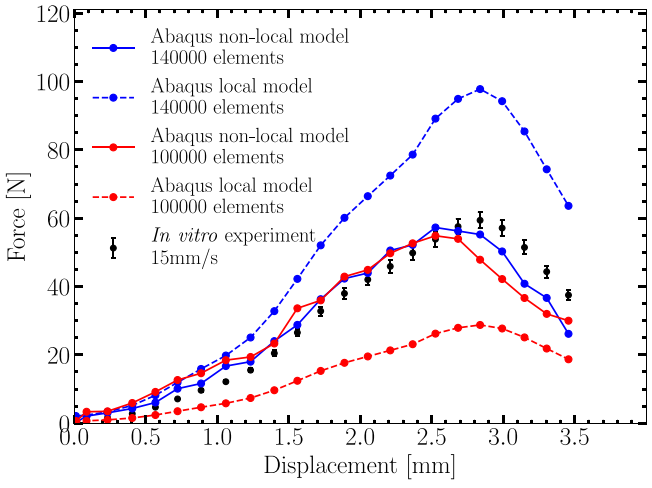

Fig. 8. Comparison between *in vitro* experimental and FE force–displacement data. The FE results include a comparison between the non-local and the local damage model for two different mesh densities. The coarse mesh has 100 000 elements, whereas the dense mesh has 140 000 elements. The coefficient of friction was $\mu = 0.8$ for these simulations.

to the study of Seupel [46] and Papadioti [45], were performed to justify the mesh objectivity of the model. In these benchmark tests, simulations were conducted on specimens with a geometry imperfection and a material imperfection that force the formation of a shear band. The shear band width was found to localise to a thin line and the damage parameter, d, increased for the same applied displacement as the mesh density increased for the local model. The mesh dependency was overcome by implementing the strain-gradient enhanced damage model where both the width of the shear band and the damage parameter remain constant for different mesh refinements [49].

Fig. 9 presents the results of the first bite model where now only one mesh density is considered (140 000 elements) and the simulations are repeated for different speeds according to the *in vitro* experiments. The results of Fig. 9 show a good agreement between the *in vitro* experiments and the non-local FE simulations, a fact that is attributed to the modified Johnson–Cook constitutive model that is used to capture the rate dependent mechanical properties of the chocolate.

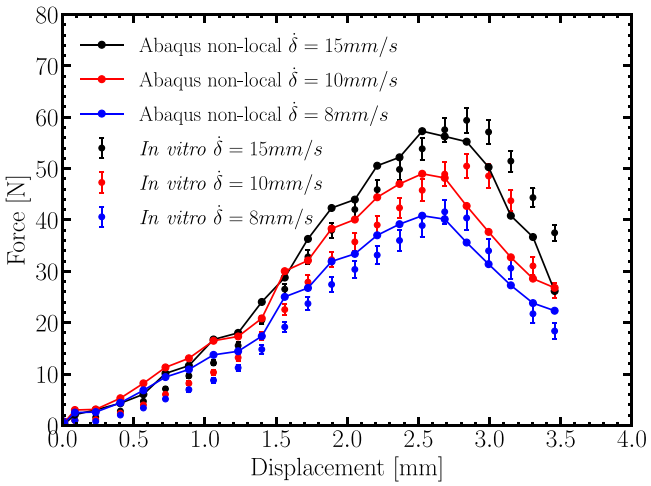

Fig. 9. Comparison between *in vitro* experimental and *in silico* FE force–displacement data for the non-aerated chocolate for different speeds. A mesh with 140 000 elements and a coefficient of friction of $\mu = 0.8$ were used for these simulations.

Fig. 10 depicts a comparison between the *in silico* FE model output and the experimental video images for different time frames A, B and C for $\dot{\delta} = 15\,\mathrm{mm\,s^{-1}}$. From Fig. 10 (stage A) it is evident that, at the point of contact between the chocolate and the teeth, the strain starts to increase leading to the crack initiation which is depicted at stage B. The strains increase further as the displacement of the lower molar teeth increases (Fig. 10 stage B) and the failure criterion is met and crack propagation initiates until complete fracture is occurred for a displacement of $\delta = 2.5\,\mathrm{mm}$ (Fig. 10, stage C). The crack that is present in the chocolate sample in the experiment, shown in Fig. 10, stage C, is captured well by the FE model.

The methodology that allows the crack propagation through element removal is well depicted in Fig. 11, where the contour plots of the equivalent plastic strain and the stress triaxiality are shown at the three time steps, A, B and C. It is worth noting here that the crack in the FE model is simulated by element removal when the damage criterion, based on the non-local equivalent plastic strain, is met. The equivalent plastic strain for the initiation of failure, depends on the stress triaxiality. For the first bite simulation, the elements that have been removed correspond to shear and tension states whereas the elements between the teeth that experience compression (negative triaxiality) can withstand higher stresses and remain in the model. By comparing the left and right column of Fig. 11, it is evident that the elements with high equivalent plastic strains, that have not been deleted from the model, are those that experience negative triaxiality, whereas those with triaxiality $\eta \geq 0$ have been deleted since the failure criterion has been met due to the high equivalent plastic strains at these triaxiality values.

5. Discussion

Our model aims to simulate the oral breakdown of chocolate due to the interaction with the molar teeth during the first bite. This model can be used to investigate how the mechanical breakdown of the chocolate can influence fragmentation, which can lead to the design of foods with better consumer perception and lower calorific value. The latter can be achieved by incorporating micro-aeration in the matrix, for which there is evidence that it also enhances the taste perception [31].

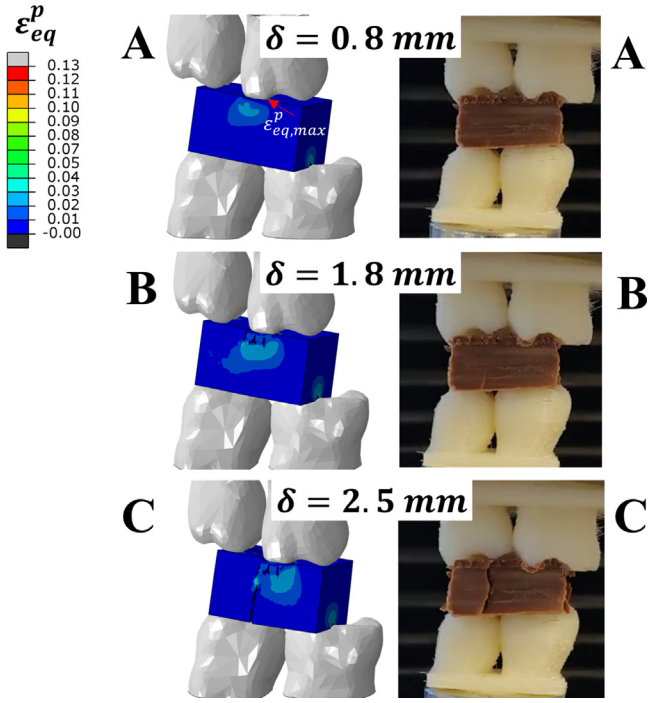

Fig. 10. Comparison between the FE simulations (left) and video frames from the *in vitro* experiment of the first bite. The frames A, B and C correspond to two intermediate steps where the penetration of the teeth into the food has started and the final fracture respectively. The displacement, δ, for each frame is also depicted. The speed was $\dot{\delta} = 15\,\mathrm{mm\,s^{-1}}$. The maximum value of equivalent plastic strain, located at the contact point with the teeth, is indicated.

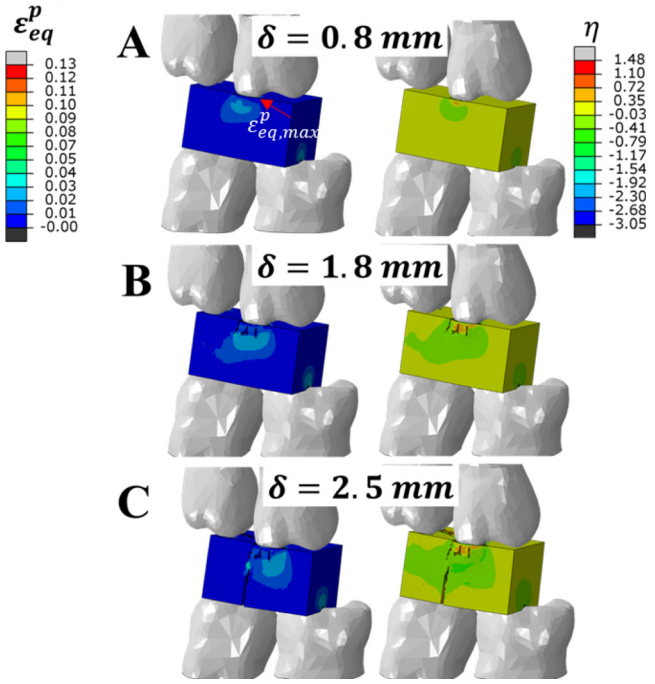

Fig. 11. The equivalent plastic strain (left) and the stress triaxiality (right) obtained through the FE simulations. The frames A, B and C correspond to the respective notation of Fig. 10. The displacement, δ, for each frame is also depicted. The speed was $\dot{\delta} = 15\,\mathrm{mm\,s^{-1}}$. The maximum value of equivalent plastic strain, located at the contact point with the teeth, is indicated.

This work supplements and expands on previous studies by undertaking both a computational and an experimental investigation. Initially, our study showed that the constitutive law used in the FE model needs to be calibrated against experimental data collected for strain rates and stress states that cover the corresponding ranges applied *in vivo*; otherwise the underlying constitutive law may not be calibrated correctly in foods exhibiting time dependent mechanical behaviour. However, *in vivo* strain rates are difficult to estimate [50], since the position of the food relative to the teeth and also the applied strain rate may vary during the first bite [51]. For this reason, the modified Johnson–Cook model was calibrated against a strain-rate range $\dot{\varepsilon} = 0.01\text{–}1\ \mathrm{s^{-1}}$. Testing at higher strain rate using hydraulic driven machines was not conducted here due to the possible dynamic effects influencing the test data, but this can be explored in the future.

It is worth focusing on the damage model applied in the current study. The modified Bai and Wierzbicki [39] damage model depends on material properties that are calculated through experiments [30]. This means that in order to predict the food fracture and damage process, the critical energy release rate, G_f, and the equivalent plastic strain, $\varepsilon^p_{eq,i}$, are required. The two additional parameters of the damage model, l and d_{cr}, were calibrated against the compression experimental data. The Bai and Wierzbicki [39] model has been extensively used in the literature to study fracture within the continuum damage framework. In our implementation of the model the critical energy release rate, G_f, is treated as a material property and not as a calibration parameter. This allows us to use the model for other materials where the G_f value is available. It is worth noting that existing studies in the literature use the damage evolution law of Eq. (3) and the G_f is used as a calibration parameter [52] or it is normalised to the element length and written as a material parameter with dimensions of critical energy per unit volume [45].

The implementation of the strain-gradient enhanced damage model imports another length scale parameter, l_{ch}, that needs to be calibrated as well. In our model, we calibrated the internal characteristic length, l_{ch}, by performing benchmark tests with induced shear band formation. A mesh sensitivity analysis was performed, and the calibrated value ($l_{ch} = 0.1\,\mathrm{mm}$) was selected so that the shear band width and the damage parameter remained constant form all mesh densities, similar to Papadioti [45] and Seupel [46]. The physical meaning of the internal characteristic length is related to the radius of the sphere around a material point over which the equivalent plastic strain is averaged. Our calibrated value lies in the range with respective values reported in the literature for metals [53–55]. In addition, the internal characteristic length, $l = 0.08\,\mathrm{mm}$, parameter of the damage model, can be related to the sugar crystal size, which lies in the same length scale (10–40 μm). The sugar crystals are visible in Fig. 12.

It is worth noting that, we simulated the first bite taking into account only the effect of the mechanical loads and the fracture of the food specimen is assumed to be caused by the contact of the teeth with the food. This is a reasonable assumption that has been adopted in the literature [40], since the fragmentation of the food during the first bite takes place in a very short time scale (∼0.5 s [56]), not allowing the thermal loads and the enzymatic reaction to influence the process. In addition, the boundary conditions i.e. the jaw trajectories, were simplified by considering a linear vector of lower jaw against the upper jaw.

Furthermore, we adopted a fully coupled thermal-stress analysis in the Explicit solver of ABAQUS [22]. As already mentioned, the temperature does not have any physical meaning in the simulation but is treated the non-local equivalent plastic strain. Although, this allows for an easy implementation of the strain-gradient enhanced framework, it constitutes a limitation of the

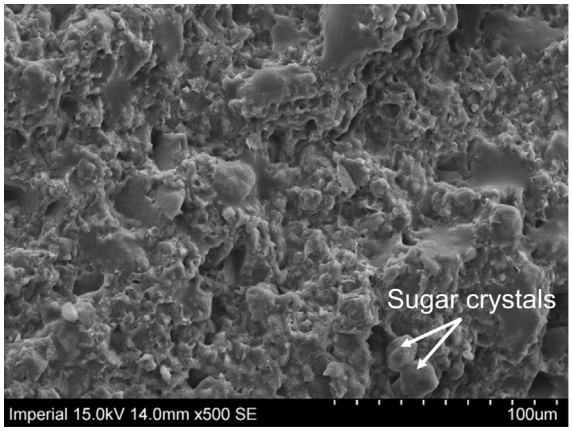

Fig. 12. SEM image of chocolate sample. More details about the SEM images and additional information appearing in them, e.g. sugar crystals, can found in Bikos et al. [30].

study since temperature cannot be used as an additional parameter that might affect the breakdown of chocolate during the first bite. The non-local damage model needs to be incorporated into the model through another technique, such as a User Element (UEL) [22] that will allow for the use of temperature as a parameter with a physical meaning in the simulation.

Although the above features could lead to a more accurate FE model, the main purpose of the current study was the implementation of a more accurate damage model that reduces the mesh dependence problem in this type of macroscopic simulations [40]. Therefore, the developed FE model can be used as a basis on which the additional parameters related to the thermal effects and chemical degradation can next be implemented. In addition, future models could include additional surfaces to represent the complete oral cavity, such that the oral process beyond the first bite may be investigated.

Our findings open new and exciting possibilities in understanding how foods fracture during the first bite, enabled through computer predictions of the effect of several parameters i.e., food texture-size-shape and contacting surface properties. Our modelling tools are generic such that they may inform food design in humans. Specifically, the models can readily be adapted to a range of food systems towards studying consumer preference, as well as the link between food fracturability and sensory perception. Moreover, the methodology presented in the current paper can be applied to study the fragmentation of foods for which the material properties are known or can be measured from experiments. Furthermore, the strain gradient enhanced damage model can be also applied to study the fragmentation of pet foods as previously reported by our group in Skamniotis et al. [5].

6. Conclusions

Our study provides a comprehensive framework for the experimental and computational investigation of the mechanical breakdown of chocolate during the first bite. Simulation of fracture is often characterised by mesh dependent results, an issue which was solved here, for the first time in foods, by implementing a strain gradient enhanced damage model.

We coupled a modified Johnson–Cook constitutive law, which was calibrated against already available compression experimental results, with a strain-gradient enhanced damage model. The framework of explicit gradient-enhanced damage model of Peerlings [43] in combination with the damage model of Bai and Wierzbicki [39] was implemented in ABAQUS Explicit through a VDFLUX subroutine. The similarities of the additional equation of Peerlings and the transient heat transfer equation allows an easy implementation in ABAQUS which needs less effort than the development of a user defined element.

The rate dependent nature of chocolate was captured in the force–displacement data of the experimental rig when three different chewing speeds were examined. The data obtained from the computational model lie in good agreement with the experimental data.

Our study highlights the superiority of non-local damage models versus commonly used local damage models in simulating food oral breakdown. The methodology can be applied to examine how differences in the structure, such as micro-aeration, can influence initially the mechanical properties and furthermore the fragmentation behaviour during the first bite. Such work is currently underway [49].

Declaration of competing interest

The authors declare the following financial interests/personal relationships which may be considered as potential competing interests: Dimitrios Bikos reports financial support was provided by Nestlé Research Center.

Data availability

Data will be made available on request.

Acknowledgements

The authors would like to acknowledge Imperial College President's PhD scholarship and the Engineering and Physical Sciences Research Council (EPSRC), United Kingdom for the financial support. This work was also supported by the Centre for Doctoral Training on Theory and Simulation of Materials (CDT-TSM) at Imperial College London. Moreover, the authors acknowledge the Nestlé PTC York for funding the project and providing the materials for testing and Dr Ruth Brooker for invaluable technical guidance during experiments.

References

[1] Simon M. Harrison, Paul W. Cleary, Towards modelling of fluid flow and food breakage by the teeth in the oral cavity using smoothed particle hydrodynamics (SPH), Eur. Food Res. Technol. 238 (2) (2014) 185–215.
[2] E. Conserva, M. Menini, T. Tealdo, M. Bevilacqua, F. Pera, G. Ravera, P. Pera, Robotic chewing simulator for dental materials testing on a sensor-equipped implant setup, Int. J. Prosthodont. 21 (6) (2008).
[3] P. Morell, I. Hernando, S.M. Fiszman, Understanding the relevance of in-mouth food processing. A review of in vitro techniques, Trends Food Sci. Technol. 35 (1) (2014) 18–31.
[4] M. Devezeaux De Lavergne, A.K. Young, J. Engmann, C. Hartmann, Food oral processing-An industry perspective, Front. Nutr. 8 (2021) 24.
[5] C. Skamniotis, Y. Patel, M.N. Charalambides, M. Elliott, Fracture investigation in starch-based foods, Interface Focus 6 (3) (2016).
[6] J. Paphangkorakit, J.W. Osborn, Effect of jaw opening on the direction and magnitude of human incisal bite forces, J. Dent. Res. 76 (1) (1997) 561–567.
[7] M. Kikuchi, T.W.P. Korioth, A.G. Hannam, The association among occlusal contacts, clenching effort, and bite force distribution in man, J. Dent. Res. 76 (6) (1997) 1316–1325.
[8] D. Tortopidis, M.F. Lyons, R.H. Baxendale, Bite force, endurance and masseter muscle fatigue in healthy edentulous subjects and those with TMD 1, J. Oral Rehabil. 26 (4) (1999) 321–328.
[9] B.K. Biswas, S. Bag, S. Pal, Biomechanical analysis of normal and implanted tooth using biting force measurement, Int. J. Eng. 4 (2) (2013) 8269.
[10] D.J. Anderson, Measurement of stress in mastication. I, J. Dent. Res. 35 (5) (1956) 664–670.
[11] S. Panda, J. Chen, O. Benjamin, Development of model mouth for food oral processing studies: Present challenges and scopes, Innov. Food Sci. Emerg. Technol. (2020) 102524.
[12] A.M. Carvalho-da-Silva, I. Van Damme, B. Wolf, J. Hort, Characterisation of chocolate eating behaviour, Physiol. Behav. 104 (5) (2011) 929–933.

[13] J.F. Meullenet, M.L. Finney, M. Gaud, Measurement of biting velocities, and predetermined and individual crosshead speed instrumental imitative tests for predicting cheese hardness, J. Texture Stud. 33 (1) (2002) 45–58.
[14] A. Sánchez-Ayala, A. Farias-Neto, N. Hellen C, R.C. Matheus Rodrigues Garcia, Relationship between chewing rate and masticatory performance, CRANIO® 31 (2) (2013) 118–122.
[15] P.H. Buschang, G.S. Throckmorton, K.H. Travers, G. Johnson, The effects of bolus size and chewing rate on masticatory performance with artificial test foods, J. Oral Rehabil. 24 (7) (1997) 522–526.
[16] E. Yoshida, K. Fueki, Y. Igarashi, Association between food mixing ability and mandibular movements during chewing of a wax cube, J. Oral Rehabil. 34 (11) (2007) 791–799.
[17] S.G. Farias Gomes, W. Custodio, F. Faot, A.A. Del Bel Cury, R.C.M. Rodrigues Garcia, Masticatory features, EMG activity and muscle effort of subjects with different facial patterns, J. Oral Rehabil. 37 (11) (2010) 813–819.
[18] G.S. Throckmorton, B.H. Buschang, H. Hayasaki, T. Phelan, The effects of chewing rates on mandibular kinematics, J. Oral Rehabil. 28 (4) (2001) 328–334.
[19] J.F. Bates, G.D. Stafford, A. Harrison, Masticatory function—a review of the literature: III. Masticatory performance and efficiency, J. Oral Rehabil. 3 (1) (1976) 57–67.
[20] S.M. Harrison, G. Eyres, P.W. Cleary, M.D. Sinnott, C. Delahunty, L. Lundin, Computational modeling of food oral breakdown using smoothed particle hydrodynamics, J. Texture Stud. 45 (2) (2014) 97–109.
[21] B. Dejak, A. Młotkowski, M. Romanowicz, Finite element analysis of stresses in molars during clenching and mastication, J. Prosthet. Dent. 90 (6) (2003) 591–597.
[22] Michael S, ABAQUS/Standard User's Manual, Version 6.17, Dassault Systèmes Simulia Corp, United States, 2017.
[23] R.J. Dorgan, A Nonlocal Model for Coupled Damage-Plasticity Incorporating Gradients of Internal State Variables at Multiscales, Louisiana State University and Agricultural & Mechanical College, 2006.
[24] N. Aravas, I. Papadioti, A non-local plasticity model for porous metals with deformation-induced anisotropy: Mathematical and computational issues, J. Mech. Phys. Solids 146 (2021) 104190.
[25] E.C. Aifantis, On the microstructural origin of certain inelastic models, J. Eng. Mater. Technol. Trans. ASME 106 (4) (1984) 326–330.
[26] E. Kröner, Elasticity theory of materials with long range cohesive forces, Int. J. Solids Struct. 3 (5) (1967) 731–742.
[27] A.C. Eringen, D.G.B. Edelen, On nonlocal elasticity, Internat. J. Engrg. Sci. 10 (3) (1972) 233–248.
[28] G. Pijaudier-Cabot, Z.P. Bažant, Nonlocal damage theory, J. Eng. Mech. 113 (10) (1987) 1512–1533.
[29] G.Z. Voyiadjis, R.J. Dorgan, A gradient enhanced, generalized plasticity/damage model: Rigorous mathematical formulation and finite element implementation, J. Mech. Behav. Mater. 15 (4–5) (2004) 309–340.
[30] D. Bikos, G. Samaras, P. Cann, M. Masen, Y. Hardalupas, C. Hartmann, J. Vieira, M.N. Charalambides, Effect of micro-aeration on the mechanical behaviour of chocolates and implications for oral processing, Food Funct. 12 (11) (2021) 4864.
[31] D. Bikos, G. Samaras, P. Cann, M. Masen, Y. Hardalupas, M.N. Charalambides, C. Hartmann, J. German, J. Vieira, Effect of structure on the mechanical and physical properties of chocolate considering time scale phenomena occurring during oral processing, Food Struct. 31 (2022) 100244.
[32] D. Bikos, G. Samaras, P. Cann, M. Masen, Y. Hardalupas, J. Vieira, C. Hartmann, P. Huthwaite, B. Lan, M.N. Charalambides, Destructive and non-destructive mechanical characterisation of chocolate with different levels of porosity under various modes of deformation, J. Mater. Sci. 58 (11) (2023) 5104–5127.
[33] A.R. Evans, M. Fortelius, Three-dimensional reconstruction of tooth relationships during carnivoran chewing, Palaeontol. Electron. 11 (2) (2008) 1–11.
[34] P.W. Lucas, D.A. Luke, Methods for analysing the breakdown of food in human mastication, Arch. Oral Biol. 28 (9) (1983) 813–819.
[35] Jianshe Chen, Food oral processing—A review, Food Hydrocolloids 23 (1) (2009) 1–25.
[36] P.W. Lucas, D.A. Luke, Optimum mouthful for food comminution in human mastication, Arch. Oral Biol. 29 (3) (1984) 205–210.
[37] C. Yven, S. Guessasma, L. Chaunier, G. Della Valle, C. Salles, The role of mechanical properties of brittle airy foods on the masticatory performance, J. Food Eng. 101 (1) (2010) 85–91.
[38] D.T. Le, J. Marigo, C. Maurini, S. Vidoli, Strain-gradient vs damage-gradient regularizations of softening damage models, Comput. Methods Appl. Mech. Engrg. 340 (2018) 424–450.
[39] Y. Bai, T. Wierzbicki, A new model of metal plasticity and fracture with pressure and Lode dependence, Int. J. Plast. 24 (6) (2008) 1071–1096.
[40] C. Skamniotis, M. Elliott, M.N. Charalambides, Computer simulations of food oral processing to engineer teeth cleaning, Nature Commun. 10 (1) (2019) 1–12.
[41] C.G. Skamniotis, M. Elliott, M.N. Charalambides, On modeling the large strain fracture behaviour of soft viscous foods, Phys. Fluids 29 (12) (2017) 121610.
[42] J. Lian, M. Sharaf, F. Archie, S. Münstermann, A hybrid approach for modelling of plasticity and failure behaviour of advanced high-strength steel sheets, Int. J. Damage Mech. 22 (2) (2013) 188–218.
[43] R.H.J. Peerlings, R. de Borst, W.A.M. Brekelmans, J.H.P. De Vree, Gradient enhanced damage for quasi-brittle materials, Internat. J. Numer. Methods Engrg. 39 (19) (1996) 3391–3403.
[44] R.H.J. Peerlings, M.G.D. Geers, R. De Borst, W.A.M. Brekelmans, A critical comparison of nonlocal and gradient-enhanced softening continua, Int. J. Solids Struct. 38 (44–45) (2001) 7723–7746.
[45] I. Papadioti, N. Aravas, J. Lian, S. Münstermann, A strain-gradient isotropic elastoplastic damage model with J3 dependence, Int. J. Solids Struct. 174 (2019) 98–127.
[46] A. Seupel, G. Hütter, M. Kuna, An efficient FE-implementation of implicit gradient-enhanced damage models to simulate ductile failure, Eng. Fract. Mech. 199 (2018) 41–60.
[47] O. Meincke, D. Kaempfer, H. Weickmann, C. Friedrich, M. Vathauer, H. Warth, Mechanical properties and electrical conductivity of carbon-nanotube filled polyamide-6 and its blends with acrylonitrile/butadiene/styrene, Polymer 45 (3) (2004) 739–748.
[48] G. Samaras, D. Bikos, J. Vieira, C. Hartmann, M. Charalambides, Y. Hardalupas, M. Masen, P. Cann, Measurement of molten chocolate friction under simulated tongue-palate kinematics: Effect of cocoa solids content and aeration, Curr. Res. Food Sci. 3 (2020) 304–313.
[49] G. Samaras, Oral Processing of Micro-Aerated Chocolates: A Computational Mechanics, Rheological and Tribological Study (Ph.D. thesis), Imperial College London, 2022.
[50] C. Swackhamer, G.M. Bornhorst, Fracture properties of foods: Experimental considerations and applications to mastication, J. Food Eng. 263 (2019) 213–226.
[51] C. Skamniotis, M. Elliott, M.N. Charalambides, On modelling the constitutive and damage behaviour of highly non-linear bio-composites–mesh sensitivity of the viscoplastic-damage law computations, Int. J. Plast. 114 (2019) 40–62.
[52] B. Wu, X. Li, Y. Di, V. Brinnel, J. Lian, S. Münstermann, Extension of the modified Bai-Wierzbicki model for predicting ductile fracture under complex loading conditions, Fatigue Fract. Eng. Mater. Struct. 40 (12) (2017) 2152–2168.
[53] S. Guo, Y. He, J. Lei, Z. Li, D. Liu, Individual strain gradient effect on torsional strength of electropolished microscale copper wires, Scr. Mater. 130 (2017) 124–127.
[54] S.P. Iliev, X. Chen, M.V. Pathan, V.L. Tagarielli, Measurements of the mechanical response of Indium and of its size dependence in bending and indentation, Mater. Sci. Eng. A 683 (2017) 244–251.
[55] P. Shrotriya, S.M. Allameh, J. Lou, T. Buchheit, W.O. Soboyejo, On the measurement of the plasticity length scale parameter in LIGA nickel foils, Mech. Mater. 35 (3–6) (2003) 233–243.
[56] H. Dan, K. Kohyama, Interactive relationship between the mechanical properties of food and the human response during the first bite, Arch. Oral Biol. 52 (5) (2007) 455–464.